

A modeling study of coastal inundation induced by storm surge, sea-level rise, and subsidence in the Gulf of Mexico

Zhaoqing Yang · Taiping Wang · Ruby Leung · Kathy Hibbard ·
Tony Janetos · Ian Kraucunas · Jennie Rice · Benjamin Preston ·
Tom Wilbanks

Received: 9 May 2013 / Accepted: 26 November 2013 / Published online: 8 December 2013
© US Government 2013

Abstract The northern coasts of the Gulf of Mexico (GoM) are highly vulnerable to the direct threats of climate change, such as hurricane-induced storm surge, and such risks are exacerbated by land subsidence and global sea-level rise. This paper presents an application of a coastal storm surge model to study the coastal inundation process induced by tide and storm surge, and its response to the effects of land subsidence and sea-level rise in the northern Gulf coast. The unstructured-grid finite-volume coastal ocean model was used to simulate tides and hurricane-induced storm surges in the GoM. Simulated distributions of co-amplitude and co-phase lines for semi-diurnal and diurnal tides are in good agreement with previous modeling studies. The storm surges induced by four historical hurricanes (Rita, Katrina, Ivan, and Dolly) were simulated and compared to observed water levels at National Oceanic and Atmospheric Administration tide stations. Effects of coastal subsidence and future global sea-level rise on coastal inundation in the Louisiana coast were evaluated using a “change of inundation depth” parameter through sensitivity simulations that were based on a projected future subsidence scenario and 1-m global sea-level rise by the end of the century. Model results suggested that hurricane-induced storm surge height and coastal inundation could be exacerbated by future global sea-level rise and

Z. Yang (✉) · T. Wang
Coastal Sciences Division, Pacific Northwest National Laboratory, 1100 Dexter Avenue North,
Suite 400, Seattle, WA 98109, USA
e-mail: zhaoqing.yang@pnl.gov

R. Leung · K. Hibbard · I. Kraucunas · J. Rice
Atmospheric Sciences and Global Change Division, Pacific Northwest National Laboratory,
3200 Innovation Blvd., K9-34, Richland, WA 99354, USA

T. Janetos
The Frederick S. Pardee Center for the Study of the Longer-Range Future, Boston University,
67 Bay State Rd, Boston, MA 02215, USA

B. Preston · T. Wilbanks
Oak Ridge National Laboratory, One Bethel Valley Road, Oak Ridge, TN 37831, USA

subsidence, and that responses of storm surge and coastal inundation to the effects of sea-level rise and subsidence are highly nonlinear and vary on temporal and spatial scales.

Keywords Coastal inundation · Storm surge · Modeling · Subsidence · Sea-level rise · Gulf of Mexico

1 Introduction

Coastal zones, although they comprise only 17 % of the US land area (<http://coastalmanagement.noaa.gov/impacts.html>), are home to more than half of the population as well as a wealth of natural and economic resources in the United States. Some of the most important energy and transportation infrastructures, ports and pipeline systems, and prestigious ecosystems are located on the northern coast of the Gulf of Mexico (GoM). Thousands of offshore oil and gas platforms exist off the Gulf coast, and about 30 % of the US oil supply and 20 % of the natural gas supply are produced in the GoM region (Minerals Management Service 2006; Staudt and Curry 2011). The low-lying areas of the Gulf coast are heavily populated and are experiencing a population shift from rural to urban and suburban areas (Burkett et al. 2008). Because many of the vital economic sectors, energy, and transportation infrastructures and large populations are located in the low-lying areas of the Gulf coast with little topographic relief, the Gulf coast is at high risk of storm surge and coastal inundation under climate change-related extreme events (Burkett et al. 2008; Needham et al. 2012).

Over the last six decades, more than 170 tropical storms have made landfall along the Gulf coast and nearly 60 of them were hurricanes (National Oceanic and Atmospheric Administration [NOAA] National Hurricane Center, <http://www.nhc.noaa.gov/pastall.shtml>). Storm surges induced by hurricanes and tropical cyclones pose significant threats to the coastal zones around the world. Hurricane-induced storm surge and coastal inundation can be significantly exacerbated by other factors such as astronomical tides, land subsidence, and climate change-related sea-level rise (SLR). Coastal vulnerability assessment studies in the GoM (Thieler and Hammar-Klose 2000; Pendleton et al. 2010) indicated that the Gulf coasts of the States of Mississippi, Louisiana, and Texas are at high to very high risk of SLR based on the “Coastal Vulnerability Index.” While high uncertainty exists in the projections of exact rates of future global SLR, it is clear that SLR at global and regional scales will result in potential impacts on coastal infrastructure, marine ecosystems, and cultural and natural resources (Nicholls et al. 2007). Land subsidence could also affect coastal inundation area and depth significantly in low-lying regions such as the northern GoM. An early study by Gornitz et al. (1991) using a hazard database indicated that the Louisiana coast and parts of the Texas coast are potentially the most vulnerable to SLR in the United States, due to anomalously high relative SLR, erosion, and land subsidence. Dixon et al. (2006) reported a maximum subsidence rate of 29 mm/year in the New Orleans area based on 2003–2005 Canada RADARSAT satellite data. Therefore, there is a strong need to study the variability of hurricane-induced storm surge and coastal inundation in the Gulf coastal regions as well as the effects of SLR and land subsidence on the surge levels under future climate conditions.

Numerical modeling has been shown to be a powerful tool for predicting storm surge and coastal inundation at desired temporal and spatial scales and resolutions. The rich data

set generated from numerical models under different climate change and land subsidence scenarios can be used to assess the risk of storm surge and provide guidance for coastal emergency management, mitigation, and adaptation. Numerous research articles have studied hurricane-induced coastal storm surge and inundation using advanced numerical models as well as statistical analysis approaches, especially since the Hurricane Katrina disaster in 2005 (Shen et al. 2006; Weisberg and Zheng 2006, 2008; Irish et al. 2008; Westerink et al. 2008; Xu et al. 2010; Dietrich et al. 2010, 2011; Mousavi et al. 2010; Tebaldi et al. 2012; Warner and Tissot 2012).

This paper presents a modeling study that simulates tides and hurricane-induced storm surges in the GoM and evaluates the effects of SLR and subsidence on the storm surge level and coastal inundation with a focus on the Mississippi River delta and the Louisiana coast. The structure of the paper is as follows. Section 2 describes the model setup, grid development, forcing mechanisms, and projections of SLR and coastal subsidence for model simulations of tide and hurricane-induced storm surge. Model results, discussion of tides, and hurricane-induced storm surges, as well as sensitivity analysis of future SLR and subsidence on storm surge, are presented in Sect. 3. Finally, a summary is provided in Sect. 4.

2 Methods

2.1 Coastal storm surge model

Unstructured-grid models have demonstrated a great advantage in simulating coastal inundation processes that require not only high grid resolution near the surge zone in the coastal region, but also a large model domain to represent the large scale and long-period forcing of hurricane wind fields (Luettich et al. 1992; Weisberg and Zheng 2006, 2008; Shen et al. 2006; Westerink et al. 2008; Bunya et al. 2010; Dietrich et al. 2010, 2011; Dawson et al. 2011; Cho et al. 2012; Kennedy et al. 2012). The storm surge model used in this study is the unstructured-grid finite-volume coastal ocean model (FVCOM) developed by Chen et al. (2003). FVCOM is a free-surface, three-dimensional primitive equations model that fully couples ice-ocean-wave-sediment-ecosystem models with options for various turbulence closure schemes, generalized vertical terrain-following coordinates, wetting–drying treatment, and data assimilation under hydrostatic and non-hydrostatic approximations. The finite-volume approach in FVCOM combines the geometric flexibility of finite-element methods with the simple and efficient computational structure of finite-difference methods. The finite-volume approach also provides better mass conservation for momentum and transport processes. The flexible unstructured-grid and mass-conservative nature make FVCOM ideally suited for interdisciplinary application in coastal oceans. FVCOM has been used to simulate tidal and estuarine circulation (Xing et al. 2011; Zheng and Weisberg 2012; Yang et al. 2012; Yang and Wang 2013), storm surge predictions (Weisberg and Zheng 2006, 2008), tidal energy extraction (Karsten et al. 2008; Yang et al. 2013), and biogeochemical processes and internal waves (Lai et al. 2010a, b; Ji et al. 2011; Wang et al. 2013).

The primitive governing equations for Reynolds-averaged turbulent flows with Boussinesq and hydrostatic approximations are represented in the following form in FVCOM:

$$\frac{\partial u}{\partial x} + \frac{\partial v}{\partial y} + \frac{\partial w}{\partial z} = 0 \tag{1}$$

$$\frac{\partial u}{\partial t} + u \frac{\partial u}{\partial x} + v \frac{\partial u}{\partial y} + w \frac{\partial u}{\partial z} - fv = -\frac{1}{\rho_o} \frac{\partial(p_h + p_a)}{\partial x} + \frac{\partial}{\partial z} \left(K_m \frac{\partial u}{\partial z} \right) + F_x \tag{2}$$

$$\frac{\partial v}{\partial t} + u \frac{\partial v}{\partial x} + v \frac{\partial v}{\partial y} + w \frac{\partial v}{\partial z} + fu = -\frac{1}{\rho_o} \frac{\partial(p_h + p_a)}{\partial y} + \frac{\partial}{\partial z} \left(K_m \frac{\partial v}{\partial z} \right) + F_y \tag{3}$$

$$\frac{\partial p_h}{\partial z} = -\rho g \tag{4}$$

where (x, y, z) are the east, north, and vertical axes in the Cartesian coordinates; (u, v, w) are the three velocity components in the $x, y,$ and z directions; (F_x, F_y) are the horizontal momentum diffusivity terms in the x and y directions; K_m is the vertical eddy viscosity coefficient; ρ is water density; p_h is hydrostatic pressure; p_a is atmospheric pressure; g is the gravitational acceleration; and f is the Coriolis parameter. To properly simulate storm surge and inundation in coastal wetland and intertidal zones, it is important to include the wetting and drying process in a storm surge model. The wetting and drying process in FVCOM is simulated using the point treatment technique based on the following criterion (Chen et al. 2008): For any given node, the node is

$$\begin{cases} \text{wet,} & \text{if } D = h + \eta > D_{\min} \\ \text{dry,} & \text{if } D = h + \eta \leq D_{\min} \end{cases} \tag{5}$$

and for any given triangular cell, the cell is

$$\begin{cases} \text{wet,} & \text{if } D = \min(h_{N1}, h_{N2}, h_{N3}) + \max(\eta_{N1}, \eta_{N2}, \eta_{N3}) > D_{\min} \\ \text{dry,} & \text{if } D = \min(h_{N1}, h_{N2}, h_{N3}) + \max(\eta_{N1}, \eta_{N2}, \eta_{N3}) \leq D_{\min} \end{cases} \tag{6}$$

where h and η are the bathymetric height and water level related to the referenced datum (North American Vertical Datum of 1988, NAVD88) in the model, respectively; $N1, N2,$ and $N3$ are the three node numbers of a triangular cell; and D_{\min} is the minimum depth criterion for wetting and drying simulation. When a triangular cell is treated as dry, the cell velocity and the fluxes across the three sides of the cell are set to zero. The total water depth in the dry cell is kept the same until the cell becomes wet again. A minimum depth (D_{\min}) of 0.05 m was used as a dry cell criterion in all simulations in this study.

In FVCOM, the wind stress is calculated as follows:

$$\bar{\tau} = C_d \rho_a \left| \bar{U}_w \right| U_w \tag{7}$$

where $\bar{\tau}$ is wind stress, ρ_a is air density, \bar{U}_w is wind velocity at 10 m height above sea surface, and C_d is the drag coefficient as a function of wind speed (Large and Pond 1981):

$$C_d = \begin{cases} 1.2 \times 10^{-3} & \left| \bar{U}_w \right| < 11.0 \text{ ms}^{-1} \\ \left(0.49 + 0.065 \left| \bar{U}_w \right| \right) \times 10^{-3} & 11.0 \text{ ms}^{-1} \leq \left| \bar{U}_w \right| < 25.0 \text{ ms}^{-1} \\ \left(0.49 + 0.065 \times 25 \right) \times 10^{-3} & \left| \bar{U}_w \right| > 25.0 \text{ ms}^{-1} \end{cases} \tag{8}$$

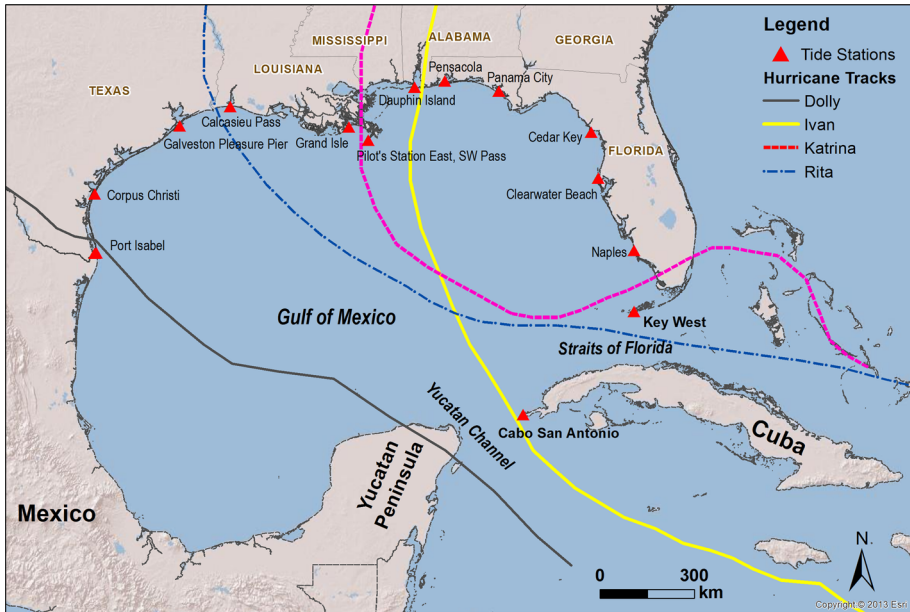


Fig. 1 Tide stations and selected hurricane tracks for model validation in the Gulf of Mexico

2.2 Model grid for the Gulf of Mexico

The GoM is a large semi-enclosed ocean basin with two narrow openings connected to the Atlantic Ocean (Fig. 1). It is connected to the Atlantic Ocean through the Straits of Florida between the United States and Cuba, and with the Caribbean Sea via the Yucatan Channel between Mexico and Cuba. Because of the circular shape of the Gulf, the shallow continental shelf occupies a significant portion of the surface area in the GoM. The Gulf coastal zones consist of large areas of wetlands, bays, barrier islands, and estuaries. Approximately, 38 % of Gulf waters are shallow intertidal areas. The deepest part of the Gulf, in the southwestern quadrant, is over 4,300 m deep, and the average water depth of the Gulf is about 1,600 m (US Environmental Protection Agency, <http://www.epa.gov/gmpo/about/facts.html>). The Gulf coast is generally low-lying with more than 80 % of the population living within 10 m of mean sea level (Gornitz et al. 1991).

An unstructured grid with triangular elements was constructed for the entire GoM using the spherical coordinate system. Because of the semi-enclosed shape of the GoM, the model open boundaries were specified at the Straits of Florida in the southeast and the Yucatan Channel in the south. The NOAA 1-arc-minute Global Relief Model (ETOPO1) bathymetric data were used to define the model water depths in the main basin of the Gulf model grid. Model bathymetry in the low-lying coastal areas and nearshore regions was interpolated from the US Geological Survey’s (USGS’s) 10-m resolution Digital Elevation Model (DEM) database. The solid land boundaries of the model are primarily defined based on the 10-m topographic contour of the USGS DEM database. There are a total of 280,667 triangular elements and 143,697 nodes in the model grid. The element sizes vary from around 300 m in the Louisiana coastal region to about 30,000 m in the center part of the Gulf (Fig. 2). Five uniformly distributed vertical layers were specified for all the model simulations.

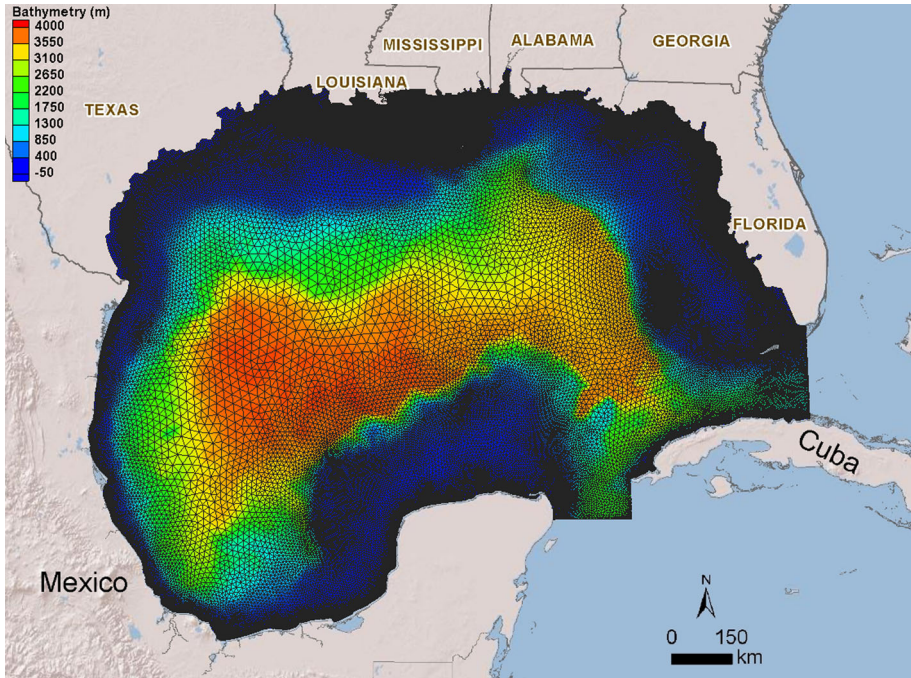


Fig. 2 FVCOM model grid and bathymetry for the Gulf of Mexico

2.3 Model forcing and boundary conditions

In this study, we focused on the coastal inundation induced by tide, relative SLR, and hurricane-induced storm surge. Flooding caused by river runoff was not considered. Salinity and temperature and their effect on density-induced circulation were also not considered. Therefore, the hydrodynamic model was run in the barotropic mode only. The model was driven by water level (i.e., tides and SLR) at the open boundaries along the Straits of Florida and the Yucatan Channel and wind and pressure fields at the water surface.

The wind field for tropical cyclones was constructed primarily based on the wind field (H^*Wind) and hurricane track data from NOAA’s Hurricane Research Division (HRD) (<http://www.aoml.noaa.gov/hrd/>) (Powell et al. 1998, 2010). The hurricane track data included hurricane center location, central atmospheric pressure, maximum sustainable wind speed, and radius of maximum wind. Because the H^*Wind field only occupies a region centered on the hurricane eye and has a radius ranging between 400 and 500 km, the wind field for the rest of the model domain outside the 500 km radius was filled with the prototypical hurricane wind field based on Holland’s method (Holland 1980). The tangential wind speed and atmospheric pressure relative to the center of a storm are determined as (Holland 1980):

$$V(r) = \sqrt{\frac{AB(P_n - P_c)\exp\left(-\frac{r}{R}\right)}{\rho_a r^B} + \left(\frac{rf}{2}\right)^2} - \frac{rf}{2} \tag{9}$$

$$P(r) = P_c + (P_n - P_c)\exp\left(-\frac{A}{r^B}\right) \tag{10}$$

$$V_m = \sqrt{\left(\frac{B}{\rho_a e}\right)(P_n - P_c)} \tag{11}$$

where r is the radial distance from the hurricane center; $V(r)$ and $P(r)$ are the tangential wind speed and atmospheric pressure at a distance of r from the hurricane center, respectively; P_n and P_c are the ambient atmospheric pressure and hurricane central pressure, respectively; A and B are hurricane shape parameters with $A = R_{\max}^B$, where R_{\max} is the radius of maximum winds; and f is the Coriolis factor. In Eq. (11), V_m is the maximum sustained wind speed and e is the base of the natural logarithm.

Following an approach similar to that of Weisberg and Zheng (2008), a linear weighting function was used to smoothly merge the H*Wind data with the Holland wind field such that the innermost region (within a radius of 400 km) near the hurricane eye was purely forced by the more accurate H*Wind data, while the outer region (beyond the H*Wind coverage radius of 500 km) was purely Holland wind. Since only atmospheric pressure data at the hurricane eye are available along the hurricane track from HRD, the hurricane pressure field was constructed using the Holland method (Eq. 10) for the entire domain based on the hurricane track data obtained from NOAA/HRD.

For tidal simulation in the GoM, eight major tidal harmonic constituents (M_2 , S_2 , N_2 , K_2 , K_1 , O_1 , P_1 and Q_1) were specified along the open boundaries based on XTide stations Cabo San Antonio and Key West, which are located at the Yucatan Channel and the Straits of Florida, respectively (Fig. 1). Tidal potential was included in the simulation. A 40-day period simulation was conducted so that the model had a sufficiently long spin-up time, with the last 30 days of that simulation period used for harmonic analysis.

For hurricane-induced storm surge simulation, a 20-day simulation was conducted, including at least 10 days before the storm made landfall. For the purpose of model validation, observed water levels at Key West station, which is maintained by the NOAA Center of Operational Oceanographic Products and Services, were used to specify the southeastern open boundary condition in the Straits of Florida. No observations are publicly available near the Yucatan Channel. Therefore, XTide predictions at Cabo San Antonio station were used in the south open boundary.

2.4 Projections of future sea-level rise and subsidence

One of the most direct impacts of global warming is the change in global mean sea level (Meehl et al. 2007). Some regional and local physical processes also contribute to the relative sea-level change. The potential impacts of relative SLR include coastal inundation, storm surge, flooding, wetland loss, saltwater intrusion, rising water table, and impeded drainage (Nicholls et al. 2011).

Relative sea-level change at a specific location is defined as the water level variation relative to the sea bed over a specific time, which can be calculated based on the contribution factors on global, regional, and local time scales (Nicholls et al. 2011):

$$\Delta RSL = \Delta SL_G + \Delta SL_{RM} + \Delta SL_{RG} + \Delta SL_{VLM} \tag{12}$$

where ΔRSL is the change in relative sea level; ΔSL_G is the change in global mean sea level; ΔSL_{RM} is the regional variation in sea level from the global mean due to meteorological and oceanographic factors; ΔSL_{RG} is the regional variation in sea level due to

changes in the earth's gravitational field; and ΔSL_{VLM} is the change in sea level due to the vertical land movement. Projection of change in SLR caused by the regional meteorological and oceanographic effects is a considerable challenge because of a lack of detailed technical guidance at the regional scale (Nicholls et al. 2011). Therefore, the regional effects of sea-level change are not considered in this study. Only contributions from the global sea-level change and land subsidence on relative sea-level change were considered in the sensitivity analysis of this paper.

Although a projected global SLR in the range of 0.18–0.6 m by the end of this century from the Intergovernmental Panel on Climate Change report has been widely cited in the past (Meehl et al. 2007), more recent research based on new future climate scenarios indicated that future global SLR could even reach 2 m by 2100 (Pfeffer et al. 2008; Vermeer and Rahmstorf 2009; Willis and Church 2012). The Coastal Protection and Restoration Authority of Louisiana (CPRA) projected 0.45 m of global SLR in the next 50 years (year 2060) and slightly above 1.0 m by the end of the century on the Louisiana coast under the less optimistic scenario developed in the Comprehensive Master Plan for a Sustainable Coast, based on information from a National Research Council study (CPRA 2012). For simplicity, we assumed 1.0 m global SLR by 2100 in the Gulf region in the SLR sensitivity analysis presented in the following section. Ranges of land subsidence rates in the Louisiana coastal region for the next 50 years were also projected by CPRA for the same less optimistic scenario, which indicated that the subsidence rate in the outer Mississippi River delta could reach as much as 25 mm/year. These land subsidence rates were used to estimate the land elevations in the Louisiana coastal region by year 2100 for the sensitivity analysis.

3 Results and discussion

3.1 Simulation of barotropic tides in the Gulf of Mexico

Tidal ranges in the Gulf of Mexico are small due to the narrow connections to the Atlantic Ocean. Tides on the Gulf coast are microtidal and mean tidal ranges are generally less than 2 m (Gornitz et al. 1991; Gouillon et al. 2010; Hill et al. 2011). Although tides are not the focus in this study, they are important in terms of coastal inundation, especially regarding interaction with storm surge in the low-lying areas of the Gulf coast. Tidal simulation in the GoM reached dynamic equilibrium after several days of spin-up, which is comparable to the spin-up time reported by Gouillon et al. (2010). Model results are presented in the form of horizontal two-dimensional (2-D) distributions of co-amplitude and co-phase in the entire Gulf basin.

Principal lunar semi-diurnal tide M_2 and diurnal tide K_1 are the two largest astronomical tidal constituents in the GoM (Hill et al. 2011). Distributions of co-amplitude and co-phase for M_2 and K_1 are shown in Fig. 3. In most of the central region of the Gulf, the M_2 amplitude is very small. M_2 amplitudes on the eastern coast of the GoM are generally greater than those on the western coast. There is an amphidromic point just north of the Yucatan Peninsula, and the phase difference around the amphidromic point varies by a complete M_2 tidal cycle. In particular, model results show four distinct regions in the Gulf with large M_2 amplitude: the southwest coast of Florida; the northwest coast of Florida; the west coast of Louisiana to the east coast of Texas; and the west coast of Yucatan Peninsula (Fig. 3), which are consistent with the model results by Hill et al. (2011) and Gouillon et al. (2010). In contrast to the M_2 amplitude, the K_1 amplitude is relatively uniform over the

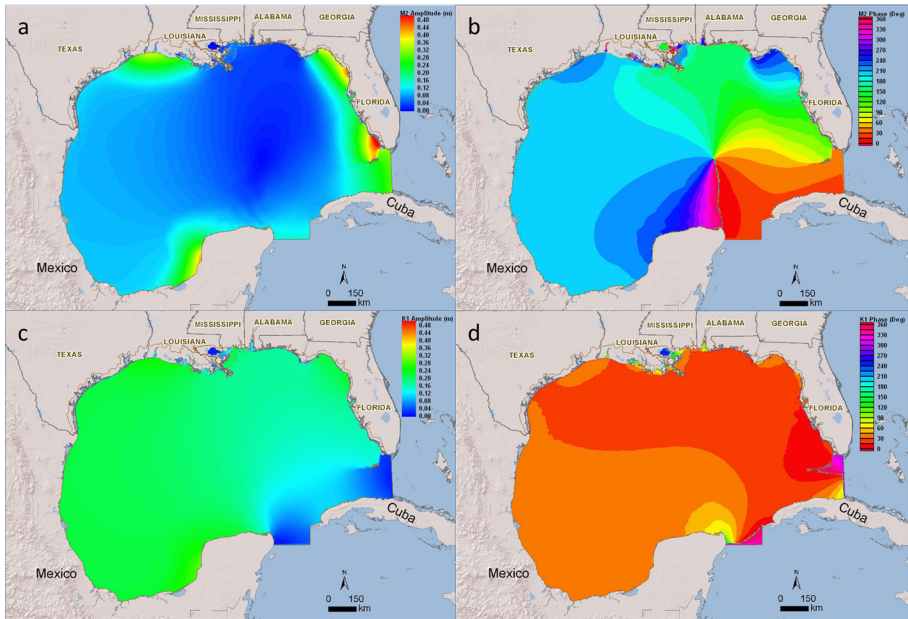


Fig. 3 Simulated co-amplitude and co-phase for semi-diurnal tide M_2 (a, b) and diurnal tide K_1 (c, d) in the Gulf of Mexico

entire Gulf, with an average value of around 0.18 m except the regions near the open boundaries (the Straits of Florida and the Yucatan Channel) where the K_1 amplitude decreases to around 0.05 m (Fig. 3). The phase difference for K_1 tide in the GoM is relatively small as well, generally within 20° , except in the Straits of Florida and the Yucatan Channel where phase differences across the channels are over 100° . The distribution patterns of tidal amplitude and phase for M_2 and K_1 in the GoM are generally in good agreement with previous modeling studies (Hill et al. 2011; Gouillon et al. 2010). It is noted that although the distribution patterns of tidal amplitude and phase in both the Straits of Florida and the Yucatan Channel are consistent with previous studies (Hill et al. 2011; Gouillon et al. 2010), errors in these regions could be larger than those in the main basin of the Gulf because of the influence of open boundary conditions.

To further validate the tidal model for the Gulf of Mexico, modeled and observed results for three largest tidal constituents (K_1 , O_1 , and M_2) were compared at selected NOAA real-time tide stations along the northern coast of the Gulf (Table 1). Locations of the real-time tide gages are shown in Fig. 1. Observed values for the harmonic constituents were directly obtained from the NOAA real-time tide Web site. Root-mean-square-errors (RMSE) were calculated for both amplitude and phase. Overall, the modeled tidal amplitudes agree with observations reasonably well, with RMSEs of 0.04, 0.033, and 0.04 m for K_1 , O_1 , and M_2 , respectively. The RMSEs for tidal phase are 10.7° , 12.1° , and 30.1° for K_1 , O_1 , and M_2 , which roughly correspond to 1-h difference between model predictions and observations for both diurnal and semi-diurnal tides. Some large errors in tidal phase predictions were mainly caused by the limitation of model grid resolution that did not resolve the detailed complexity of the shoreline, barrier islands, and small bays and inlets in the Gulf (Gouillon et al. 2010). Because the main objective of the study is on the coastal inundation induced

Table 1 Comparison of tidal amplitude (m)/phase (degree) between observations and model results (*italics*) at NOAA real-time tide gage stations in the Gulf of Mexico

Stations	K_1	O_1	M_2
Port Isabel, TX	0.137/39.5 <i>0.210/30.6</i>	0.137/31.8 <i>0.200/32.3</i>	0.062/277.4 <i>0.097/222.7</i>
Corpus Christi, TX	0.210/24.5 <i>0.160/30.0</i>	0.200/16.8 <i>0.162/31.6</i>	0.106/260.1 <i>0.083/215.5</i>
Galveston Pleasure Pier, TX	0.171/28.0 <i>0.230/34.5</i>	0.161/20.3 <i>0.200/35.2</i>	0.139/276.1 <i>0.230/246.9</i>
Calcasieu Pass, LA	0.144/29.8 <i>0.181/31.1</i>	0.136/22.3 <i>0.159/38.8</i>	0.146/254.7 <i>0.230/241.9</i>
Grand Isle, LA	0.114/37.4 <i>0.127/40.9</i>	0.114/30.8 <i>0.127/34.5</i>	0.013/163.0 <i>0.032/165.2</i>
Pilot's Station East, SW Pass, LA	0.133/20.6 <i>0.175/22.4</i>	0.132/12.0 <i>0.171/25.5</i>	0.017/123.0 <i>0.034/159.1</i>
Dauphin Island, AL	0.141/50.6 <i>0.100/58.9</i>	0.138/41.9 <i>0.108/50.0</i>	0.015/132.5 <i>0.021/162.1</i>
Pensacola, FL	0.154/52.2 <i>0.174/22.7</i>	0.151/42.3 <i>0.170/26.0</i>	0.025/170.3 <i>0.031/152.1</i>
Panama City, FL	0.141/37.5 <i>0.173/22.2</i>	0.135/28.1 <i>0.166/24.1</i>	0.026/139.1 <i>0.022/151.0</i>
Cedar Key, FL	0.177/34.6 <i>0.209/31.7</i>	0.163/27.6 <i>0.198/33.2</i>	0.386/189.5 <i>0.367/210.8</i>
Clear Water, FL	0.158/12.4 <i>0.184/14.2</i>	0.151/3.6 <i>0.171/19.7</i>	0.246/123.1 <i>0.231/154.7</i>
Naples, FL	0.158/9.9 <i>0.163/12.7</i>	0.143/2.8 <i>0.156/16.9</i>	0.286/144.2 <i>0.320/116.1</i>
RMSE	0.040/10.7	0.033/12.1	0.040/30.1

by storm surge, sea-level rise, and land subsidence, the accuracy of tide prediction is considered sufficient for the purpose of this study.

3.2 Simulation of storm surges induced by hurricanes

To demonstrate the model's capability for simulating storm surges induced by hurricanes along the northern Gulf coast, model simulations of storm surges forced by historical hurricane wind and pressure fields were conducted. Four historical hurricanes, including Ivan (2004), Katrina (2005), Rita (2005), and Dolly (2008), which made landfalls along the northern Gulf coast, were selected for simulation based on the consideration of data availability, hurricane intensity, and landfall locations. The tracks and key characteristics of the four hurricanes are given in Fig. 1 and Table 2, respectively.

Hurricane Ivan was a long-lived Category 5 hurricane, according to the Saffir-Simpson Hurricane Wind Scale (NOAA/NWS 2012), which made landfall three times along the US Coast. It made the first landfall near Gulf Shores, Alabama, as a strong Category 3 hurricane around 0700 Coordinated Universal Time (UTC) on September 16, 2004, with 195 km/h winds. The impact of the associated storm surge was magnified by its

Table 2 Hurricane characteristics near the time of landfall

Hurricane	Time (UTC)	Location (lon, lat)	Pressure (mb)	Max. Wind Speed (km/h)
Ivan	0650 UTC 16 Sep 2004	(−87.9, 30.2)	946	195
Katrina	1110 UTC 29 Aug 2005	(−89.6, 29.3)	920	205
Rita	0740 UTC 24 Sep 2005	(−93.7, 29.7)	937	220
Dolly	1820 UTC 23 July 2008	(−97.2, 26.4)	967	140

coincidence with high tide. Hurricane Katrina was the costliest hurricane in US history and the deadliest and most destructive hurricane of the 2005 Atlantic hurricane season. Katrina approached the Mississippi shelf as a Category 5 hurricane before degrading to Category 3 when it made landfall at 1110 UTC on August 29, 2005, along the southern reach of the Mississippi River in Louisiana. Due to its especially large size and unique landfall location, Katrina brought massive damage and flooding to the City of New Orleans. Hurricane Rita was another Category 5 hurricane of the 2005 hurricane season and struck the Gulf coast a few weeks after Katrina's landfall. Rita made landfall near the border between Texas and Louisiana on September 24, 2005, as a Category 3 hurricane with winds at 195 km/h and quickly weakened after the landfall. Hurricane Dolly was one of the few hurricanes that made landfall along the northwestern coast of the GoM and the second most destructive US hurricane that occurred in the month of July. Dolly made landfall on South Padre Island, Texas, at 1800 UTC July 23, 2008, as a Category 1 hurricane, with 140 km/h sustained winds.

Simulations of the storm surge induced by all four selected hurricanes were compared to observed water levels at NOAA tide stations that are closest to the hurricane tracks (or landfall locations) (Fig. 1). Modeled and observed storm surge heights were compared at two NOAA tide stations on both side of the hurricane track for all four hurricanes. Time-series comparisons of water levels during hurricanes are provided in Fig. 4. It can be seen in general that simulated water levels match the field observations reasonably well. The model captured the peak surge heights at most of the stations. It should be noted that observed data and model results only show about 2 m surge height for Hurricane Katrina (Fig. 4a) because Pilot's Station East is far offshore from the location of maximum surge height, which occurred near the mouth of Bay St. Louis. Maximum surge heights of 8.45 m and 7.83 m were recorded at Pass Christian and Long Beach, respectively (http://www.wunderground.com/hurricane/surge_us_records.asp?MR=1), where the model hindcasted maximum surge heights of 8.01 m at Pass Christian and 7.58 m at Long Beach. The model underpredicted the peak surge height by about 0.4 m at Pilot's Station East during Katrina (Fig. 4a). The misfit was mainly caused by two factors. The first was that the channel of Southwest Pass and the nearby levee were not very well represented in the model because of the grid resolution. The tide gage was located at the southeast end of the Pass and was subject to strong onshore wind that resulted in higher water levels along the shore during Hurricane Katrina. However, the nearest model grid point near the gage was off the south end of Southwest Pass and therefore the model under-predicted the surge height. The other factor is the uncertainty of the wind field. In this study, wind

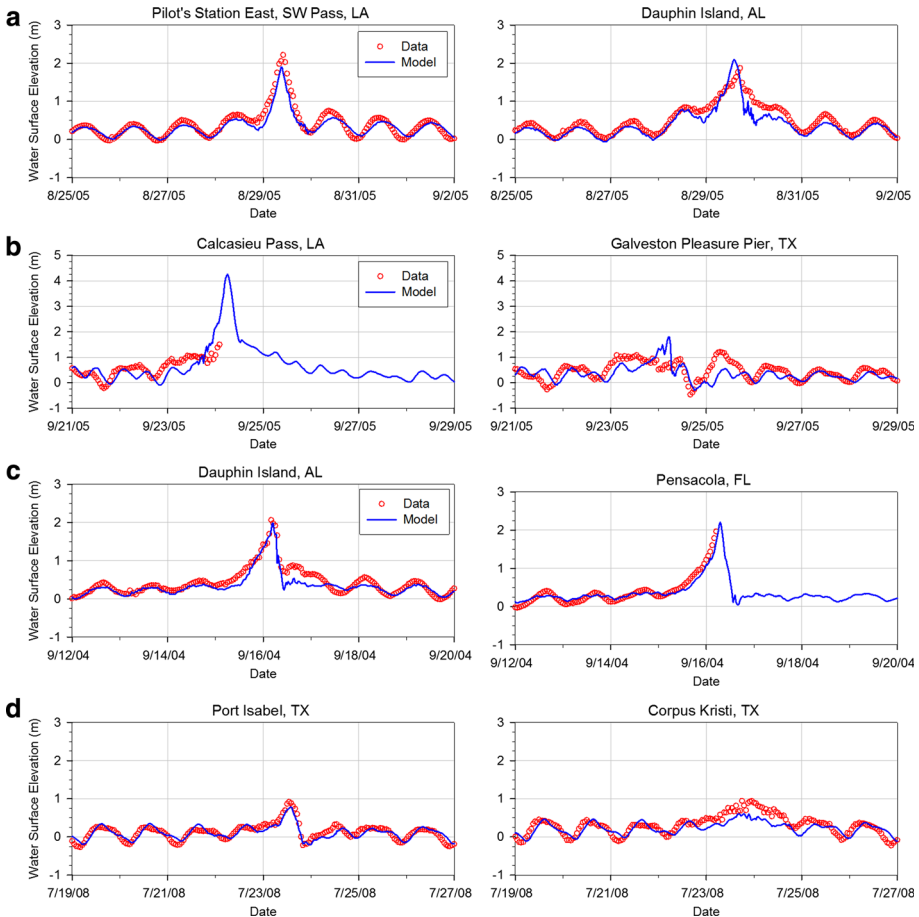


Fig. 4 Comparison of modeled and observed storm surge levels during hurricane events **a** Katrina; **b** Rita; **c** Ivan; and **d** Dolly. Note: Some data were not available due to damage of tide gage at Calcasieu Pass, LA, during Hurricane Rita and Pensacola, FL during Hurricane Ivan

forcing was constructed based on a combination of $H \cdot \text{Wind}$ for an inner core region of 400 km radius and Holland wind for the outer region. The approach may lack the accuracy in the merging area between the inner and outer regions for large hurricanes, such as Katrina, in which sustained tropical-storm-force wind extended outward up to 370 km from the hurricane center (Graumann et al. 2005, Powell et al. 2010). Furthermore, three-hourly intervals of wind field may not be sufficient to accurately represent the temporal variations of hurricane wind forcing, as shown in studies by Dietrich et al. (2010, 2011), in which 30-min intervals of Katrina wind field were used. Although observed data were missing during the period of peak surge at Calcasieu Pass station because the tide gage was damaged during Hurricane Rita (Fig. 4b), post-hurricane surge level records indicated that the maximum storm surge height during Hurricane Rita was 4.57 m near the city of Calcasieu Pass, LA (<http://water.weather.gov/ahps2/crests.php?wfo=lch&gage=capl1>), which is close to the hindcasted maximum surge height of 4.27 m. There was no distinct surge signal in the observed data at Galveston Pleasure

Pier during Hurricane Rita, but the model showed a small surge. The misfit was likely caused by the model grid resolution that was not fine enough to revolve the complex shoreline of Galveston Bay. There is also a possibility of errors in the data because of the irregular time history as shown in the right panel of Fig. 4b. Similarly, the model failed to capture the slowly dropping water level after the landfall of Hurricane Ivan (Fig. 4c) because the model grid was not able to represent the tide gage location at the northeast side of Dauphin Island, which was subject to offshore wind after hurricane landfall. Clearly, model results can be further improved by refining the model grid, especially near the tide gage locations. But the resolution is sufficient for the purpose of this study, which emphasizes the effects of storm surge, sea-level rise, and subsidence on coastal inundation. Simulated storm surge heights during Hurricane Dolly matched the observed data well although model results were slightly lower than the data at Corpus Kristi Station (Fig. 4d).

Figure 5 shows snapshots of wind fields and simulated water levels during Hurricane Katrina. As one can see, the spatial distributions of water level height are closely correlated with the wind field. For instance, higher storm surge tends to develop at the right side of the hurricane track where the wind speed is strongest and wind direction is toward the shore. In contrast to the left side of the hurricane track, water level is lowered as winds blow the water offshore. Figure 5a, b shows the Hurricane Katrina wind field and induced surge height at 0600 UTC August 29, 2005, 6 h before landfall. As Hurricane Katrina approached the shore, water level was elevated on the east side of the Mississippi River delta (right side of Katrina track) and decreased on the west side of the river (left side of Katrina track). When Katrina made landfall at 1200 UTC August 29, 2005 (Fig. 5c), strong onshore winds occurred in the coastal region east of the Mississippi River delta, resulting in storm surge height over 6 m during the landfall (Fig. 5d).

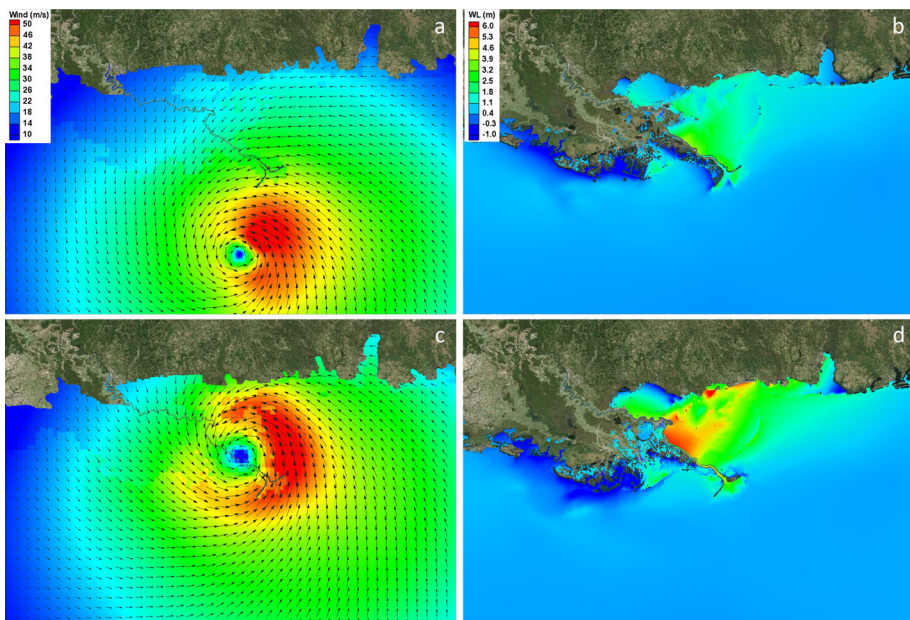


Fig. 5 Hurricane Katrina wind field and induced storm surge along the eastern Louisiana coast at 0600 UTC, Aug 29, 2005 (a, b) and 1200 UTC, Aug 29, 2005 (c, d). Water level is referred to NAVD88

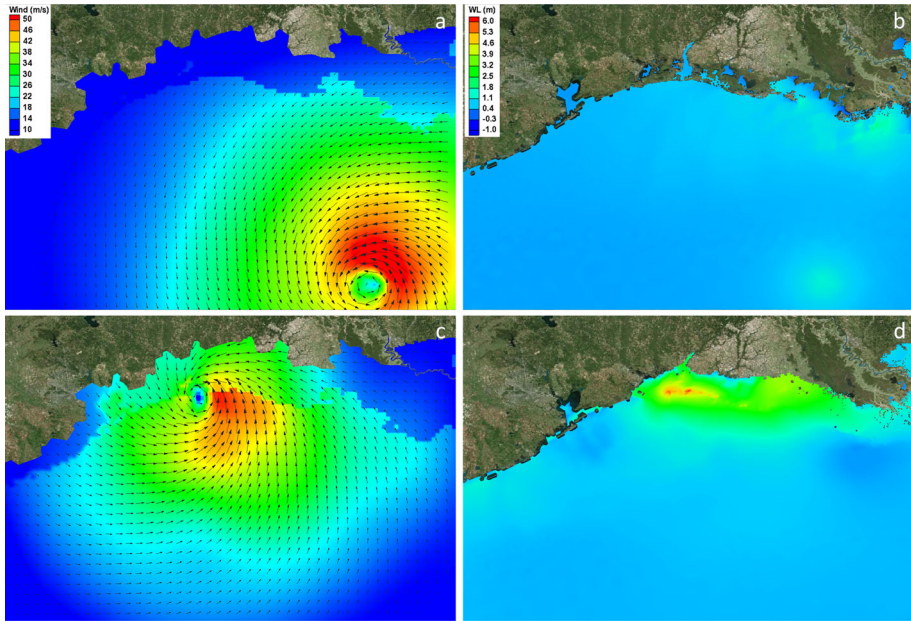


Fig. 6 Hurricane Rita wind field and induced storm surge along the western Louisiana coast at 1200 UTC, Sept 23, 2005 (a, b) and 0730 UTC Sept 24, 2005 (c, d). Water level is referred to NAVD88

Compared to Hurricane Katrina, the speed of Hurricane Rita was much slower as it approached the northern coast of the Gulf. Figure 6a, b shows the Hurricane Rita wind field and induced surge height at 1200 UTC September 23, 2005. Although it was about 20 h before landfall, water started to surge along the western Louisiana coast (Fig. 6b). During the landfall of Hurricane Rita around 0730 UTC September 24, 2005 (Fig. 6c), strong storm surge occurred in a broad area along the western Louisiana coast as a result of strong onshore (northward) winds (Fig. 6d). To the left side of the hurricane eye, water level along the coastline was actually suppressed by the offshore winds. It is also seen that large areas were inundated along eastern Texas and western Louisiana coasts during Hurricane Rita's landfall (Fig. 6d) in comparison with the condition before landfall (Fig. 6b).

3.3 Effects of SLR and land subsidence

To evaluate the effects of global SLR and localized land subsidence on coastal inundation during storm surge events in the GoM, sensitivity simulations were conducted based on the projections of SLR and subsidence rates described in Sect. 2.4. Three sensitivity runs were conducted, including SLR only, subsidence only, and combined SLR and subsidence. To simulate the effect of global SLR, we used the approach by Mariotti et al. (2010) and Mousavi et al. (2010) to superimpose the rate of 1-m rise by the end of the century on tidal elevations at the open boundaries. The effect of land subsidence was simulated by modifying the model bathymetry to reflect the land subsidence, with the assumption that subsidence rates along the Louisiana coast by the end of the century remain the same as those for the next 50 years estimated by CPRA (2012). Figure 7 shows the change of model bathymetry in the Mississippi River delta between the baseline and the subsidence

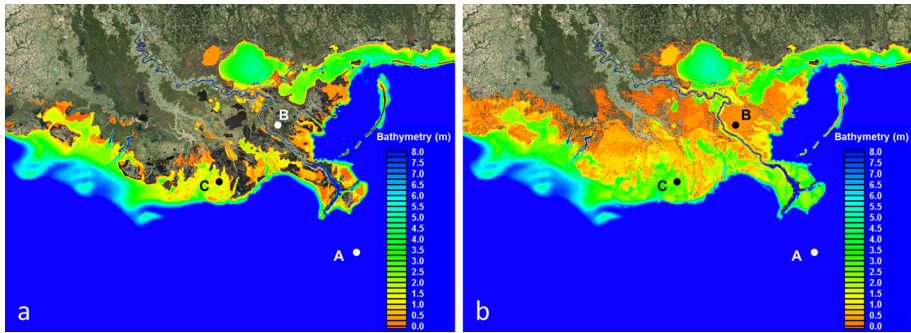


Fig. 7 Comparison of bathymetry height between baseline (a) and subsidence condition (b). The circles labeled with A, B, and C denote the three sites for subsequent water level analysis in Figs. 10, 11, and 12

condition. A substantial change in water depth and water coverage area as a result of land subsidence can be seen. This change could have broader impact on coastal inundation because it not only affects the subsidence areas but also makes adjacent upland regions more vulnerable to coastal flooding. For all the sensitivity runs, the same wind and pressure forcing of Hurricane Katrina used in the baseline condition were applied.

Figure 8a–c shows the coastal storm surge height and inundation area for scenarios of SLR, subsidence, and combined SLR and subsidence under the same wind forcing as Hurricane Katrina. Compared to the baseline condition (Fig. 5c), water level and inundation area for the 1-m SLR scenario increase significantly in the entire Mississippi Delta region (Fig. 8a). However, for the subsidence scenario (Fig. 8b), although more areas are inundated due to land subsidence, water level on the west side of the delta and hurricane track (Fig. 1) actually becomes lower than the baseline condition because strong offshore wind blows the water offshore such that the water level is close to the subsided water bottom, which is lower than the baseline condition. For the combined SLR and subsidence scenario (Fig. 8c), water level on the east side of the delta and hurricane track increase even more than in the SLR scenario because more water is available to be pushed toward the shore by the onshore hurricane wind. On the other hand, water level on the west side of the delta and hurricane track is lower than the SLR scenario, similar to the result for the subsidence scenario due to the same mechanism of strong offshore wind.

To better illustrate the changes of coastal inundation between a sensitivity run and the baseline condition, the change of inundation depth (ΔD_{inund}) at a model grid node was used in the analysis, and is defined as follows:

$$\Delta D_{inund} = \begin{cases} \Delta D - \Delta h & \text{if a node is wet in both runs} \\ 0 & \text{if a node is dry in both runs} \\ \Delta D & \text{if a node is dry in one of the runs} \end{cases} \quad (13)$$

where ΔD is the difference of total water depth between the sensitivity run and the baseline condition at the grid node; Δh is the difference of bathymetry height between the sensitivity run with subsidence effect and the baseline condition. Based on the definition (Eq. 13), one can see that ΔD_{inund} represents the net change of inundation depth at a model grid node between the sensitivity run and the baseline condition.

The spatial distributions of change of inundation depth (ΔD_{inund}) near the Mississippi River delta for the three sensitivity runs were calculated to illustrate the effects of SLR and land subsidence on coastal inundation (Fig. 9). Figure 9a, b shows the distribution of

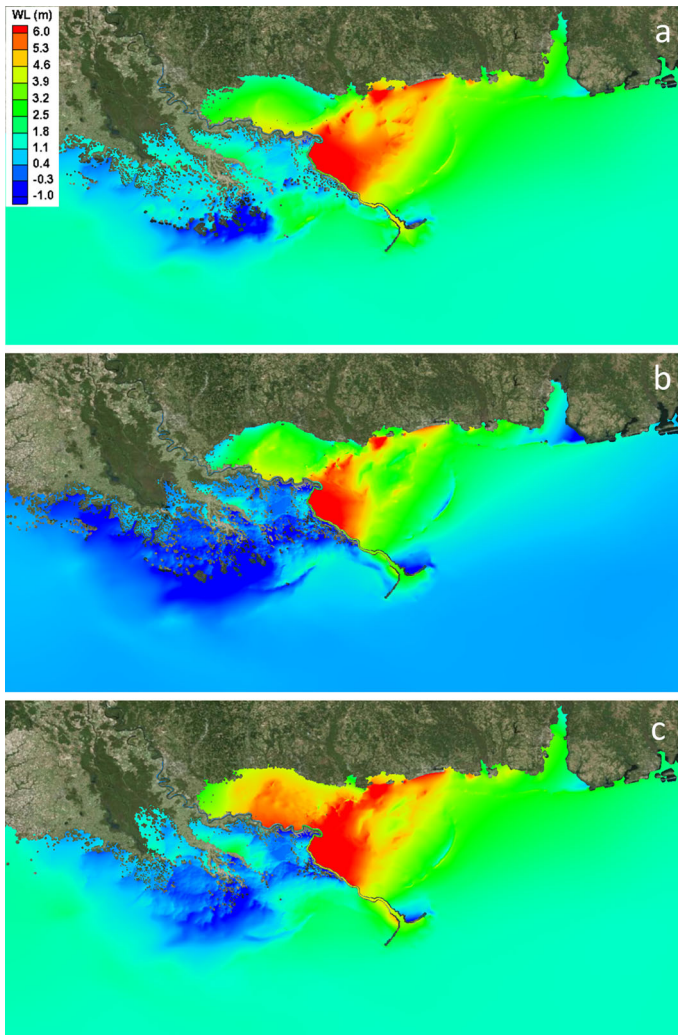


Fig. 8 Simulated hurricane-induced coastal inundation for **a** SLR scenario, **b** subsidence scenario, and **c** combined effect of SLR and subsidence. Water level is referred to NAVD88

ΔD_{inund} for the 1-m SLR scenario at 6 h before the landfall and at the time of landfall. In most of the areas, especially offshore, ΔD_{inund} is very close to 1 m, which is primarily attributed to the 1-m SLR imposed at the open boundaries. However, in shallow areas near the delta, ΔD_{inund} shows substantial spatial variations caused by the hurricane wind field and nonlinear effects. In general, water tends to pile up to the east side of the Mississippi River, corresponding to the onshore wind direction, as indicated by areas with $\Delta D_{\text{inund}} > 1$ m. In comparison with the west of the Mississippi River, water is pushed away offshore, as indicated by areas with $\Delta D_{\text{inund}} < 1$ m. As the hurricane approaches landfall (Fig. 9b), the change of inundation depth (ΔD_{inund}) becomes even larger and occurs in more areas near shore, as compared to the condition 6 h before landfall (Fig. 9a). In contrast, the

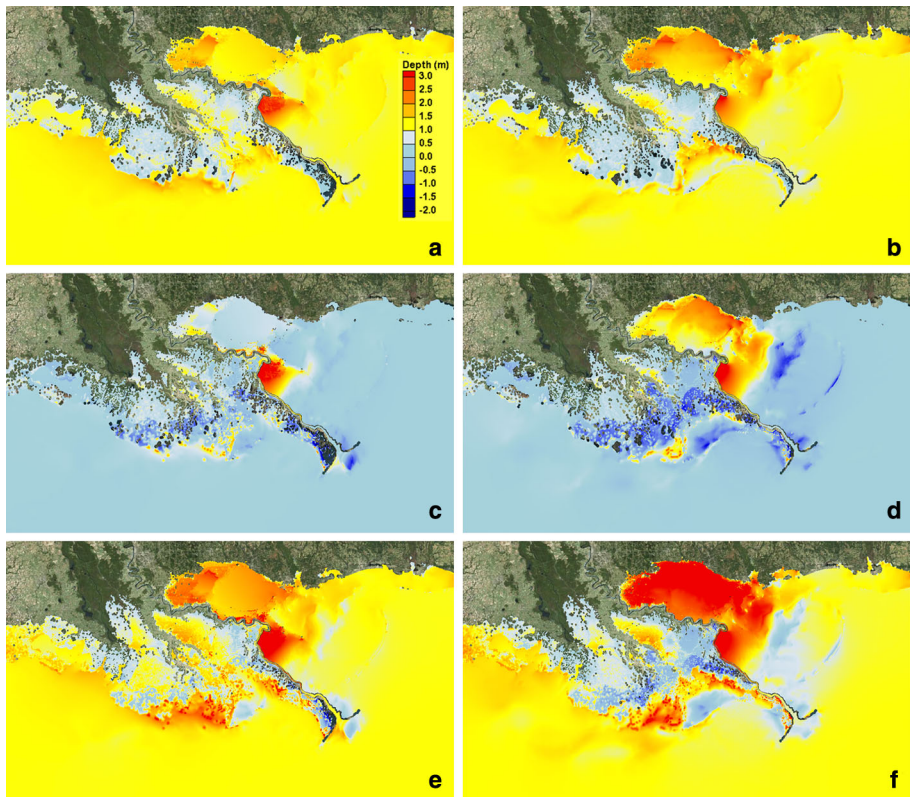


Fig. 9 Simulated change of inundation depth. *Upper panels:* 1-m SLR scenario at **a** 6 h before hurricane’s landfall and **b** during hurricane’s landfall. *Middle panels:* subsidence scenario at **c** 6 h before hurricane’s landfall and **d** during hurricane’s landfall. *Lower panels:* scenario with combined effect of 1 m SLR and land subsidence at **e** 6 h before hurricane’s landfall and **f** during hurricane’s landfall

change of inundation depth (ΔD_{inund}) for the subsidence scenario during the hurricane event is close to zero in most of the deep area in the Mississippi Delta (Fig. 9c, d). However, local variations of inundation depth are seen in the shallow region where inundation depth tends to increase on the east side of the hurricane track and decrease on the west side of the track.

The change of inundation depth (ΔD_{inund}) shows even stronger nonlinear response to the combined effect of SLR and land subsidence (Fig. 9e, f) in comparison with the SLR scenario (Fig. 9a, b). The combined effect of global SLR and subsidence substantially increased the total water depth in many areas that are either very shallow or even dry in the baseline condition (see also Fig. 7). The increase in water depths as well as in wetting areas intensify the storm surge potential and results in greatly increased inundation depth in shallow regions that are subject to strong onshore winds during the hurricane. As seen in Fig. 9e, f, inundation depths in the nearshore regions (e.g., Lake Pontchartrain) increase significantly both at 6 h before and during the hurricane’s landfall. It should be pointed out that the severity of inundation in the Lake Pontchartrain area may be over-predicted due to the lack of sufficient grid resolution to resolve the fine-scale levee structures in the model.

To evaluate the effects of SLR and subsidence on the temporal evolution of storm surge and coastal inundation, time series of water levels are compared between sensitivity runs

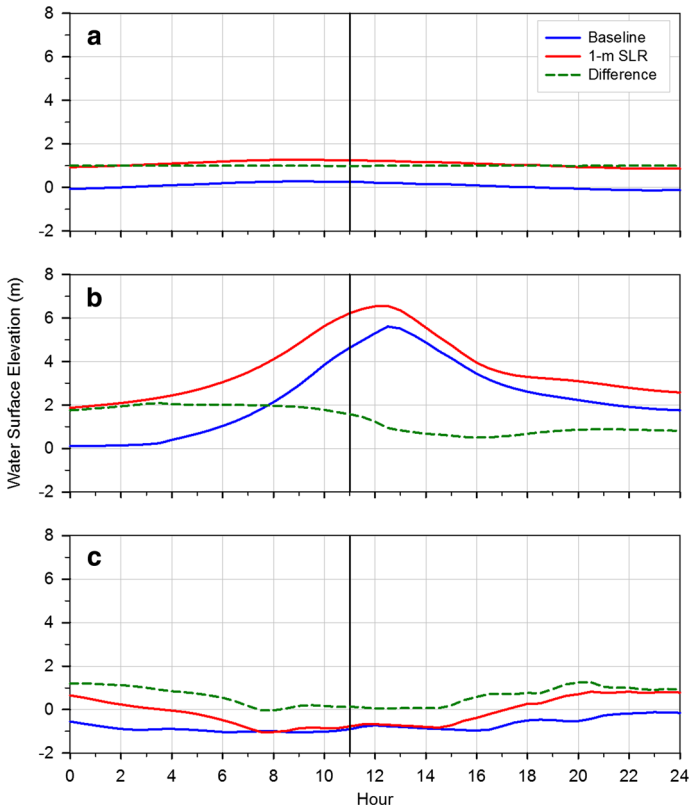


Fig. 10 Comparisons of water level time series at Sites A (a), B (b), and C (c) between baseline condition and 1-m SLR. The vertical black lines denote the hurricane's landfall time around 11 a.m

and the baseline condition at three sites around the Mississippi River delta. As shown in Fig. 7, Site A is located offshore with water depth greater than 100 m. Site B is within the intertidal zone on the east side of the Mississippi River and the hurricane track, a region that experienced strong surge during hurricane landfall. In contrast, Site C is located in a shallow embayment to the west of the Mississippi River and experienced water set down during hurricane landfall.

Figure 10a–c shows the time series of water levels between baseline and SLR scenarios and their differences at Sites A, B and C. Clearly, at the offshore Site A (Fig. 10a), water level for the 1-m SLR scenario basically equals to the sum of the baseline water level and the 1-m SLR that was imposed at the open boundaries, indicating a linear relationship between SLR scenario and baseline conditions in the offshore region. In contrast, storm surge heights at Sites B and C show strong nonlinear responses to the effect of SLR. At Site B (Fig. 10b), there is a noticeable phase difference in the peak surge between the baseline and SLR conditions. Under the SLR condition, the surge wave propagated slightly faster than that in the baseline condition, presumably due to the increase in water depth from SLR. As indicated by the time-series difference of water levels in Fig. 10b, the effect of 1-m SLR also resulted in a greater increment of inundation depth (nearly 2 m) at Site B before the hurricane landfall, which is consistent with the horizontal 2-D plot of the change of inundation depth ($\Delta D_{\text{inund}} > 1$ m, as shown in Fig. 9a, b). Compared to Site B, the water

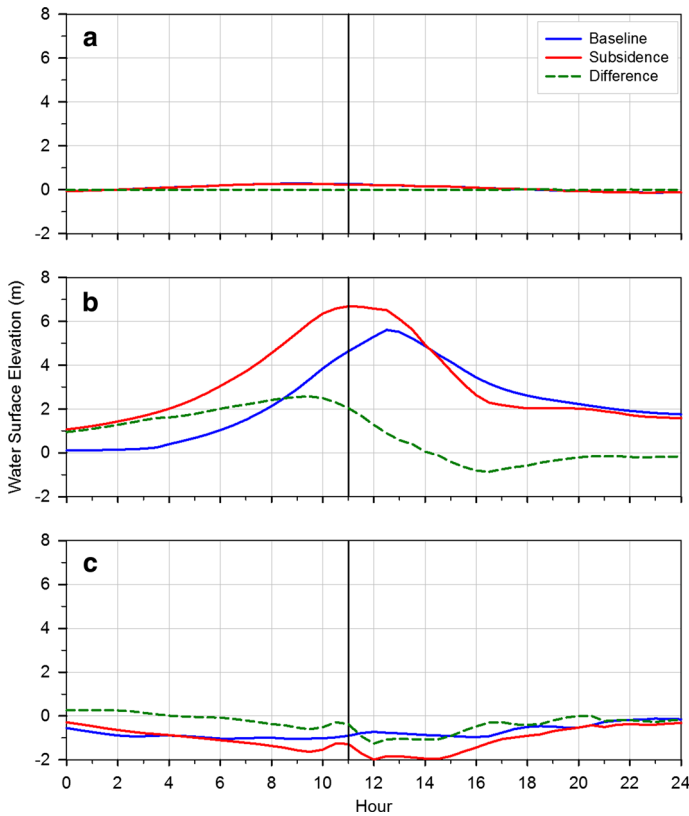


Fig. 11 Comparisons of water level time series at Sites A (a), B (b), and C (c) between baseline condition and subsidence scenario. The vertical black lines denote the hurricane’s landfall time around 11 a.m

level at Site C is reduced nearly to the baseline level because Site C is on the west side of the hurricane track where water mass is being blown away by the strong offshore wind, resulting in a water level close to the baseline condition despite the 1-m sea-level rise. Consequently, the water level differences between the baseline and SLR conditions were smaller than 1 m and even close to 0 during the landfall period.

Figure 11a–c shows the time series of water levels between the subsidence scenario and baseline condition at Sites A, B, and C. Again, change in water level at Site A is nearly zero (Fig. 11a). At Site B (Fig. 11b), the peak of the surge level happens earlier than the baseline condition, likely caused by faster wave propagation speed in deeper water, resulting in a large increase in inundation depth right before landfall and decrease right after landfall. At Site C (Fig. 11c), water level drops even below the baseline condition because Site C is not only in the offshore wind region, similar to the condition of the 1-m SLR scenario, but also in the subsidence region where bathymetry height is lower than the baseline condition. Therefore, water level is further set down by the hurricane wind. These results are consistent with the 2-D distribution of water level (Fig. 8b) and change in inundation depth shown in Fig. 9c, d.

Time-series distribution of water levels for the scenario of combined SLR and subsidence at Site A (Fig. 12a) has a pattern similar to that of the SLR-only and subsidence-only

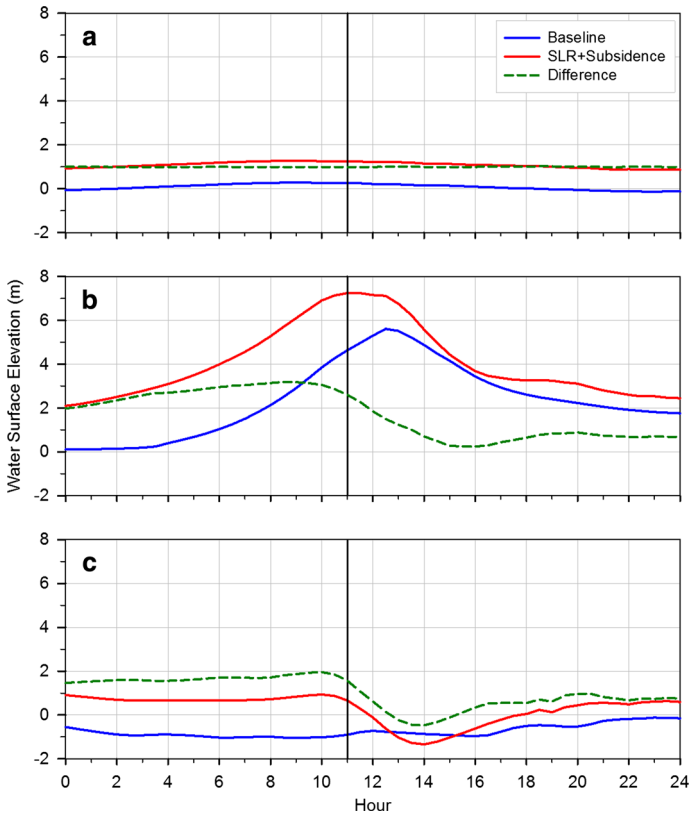


Fig. 12 Comparisons of water level time series at Sites A (a), B (b), and C (c) between baseline condition and the scenario with combined effects of 1-m SLR and land subsidence. The vertical black lines denote the hurricane's landfall time around 11 a.m

scenarios. However, water level at Site B is much more elevated, and the phase shift of peak surge becomes more evident due to the combined effects of SLR and land subsidence (Fig. 12b) in comparison with the SLR-only or subsidence-only scenarios (Figs. 10b, 11b). Water level differences are generally larger than 2 m at Site B for the period prior to the hurricane's landfall. At Site C, although water level in the combined SLR and subsidence scenario is generally higher than the baseline condition due to the combined effect of SLR and land subsidence, it still drops below the baseline level after the hurricane's landfall (hours 13–15 in Fig. 12c), as a result of lower bathymetry height and the strong offshore hurricane wind.

Model results shown in Figs. 10 and 12 suggested that the effects of SLR and subsidence can exacerbate the storm surge height, the timing of the peak surge, and inundation areas in the nearshore regions during a hurricane. The response of storm surge and coastal inundation to these effects is nonlinear and varies temporally and spatially. However, in the offshore deep-water regions, the effect of subsidence on storm surge is negligible and the effect of SLR is just a linear addition to the storm surge height.

4 Summary

In an effort to understand the effects of global SLR and local subsidence on coastal inundation during extreme storm surge events, an unstructured-grid coastal ocean model, FVCOM, was applied to simulate tides and hurricane-induced storm surges in the northern GoM. A series of sensitivity runs were also conducted to further evaluate the effects of SLR and subsidence on coastal inundation. The comparisons of model results to field observations for four selected historical hurricanes (Katrina, Rita, Ivan, and Dolly) demonstrated that the model can simulate tides and storm surges reasonably well in the GoM. Model results suggested that storm surge height and coastal inundation induced by hurricanes could be exacerbated by future global SLR and land subsidence. Effects of global SLR and land subsidence on storm surge and coastal inundation are highly nonlinear and vary on temporal and spatial scales, which could either increase or reduce the inundation depth substantially, depending on the location of the coastal zone relative to the hurricane track.

While this study presents interesting and important findings about the effects of SLR and land subsidence on coastal inundation during storm surge events, the model can be improved to increase the accuracy of storm surge prediction in the northern Gulf coast and reduce the uncertainties of the findings. For example, the model grid resolution can be further refined to better represent the coastal features, such as channels, embayments, and barrier islands, which are important to the accuracy of prediction of storm surge height and inundation area (Dietrich et al. 2010). Wave effect was not included in this study. Consideration of wind-driven wave interaction with storm surge in model simulation would improve the prediction of storm surge as suggested by Sheng et al. (2010) and Dietrich et al. (2011). Tidal boundary conditions were specified using XTide in this study. It is necessary to explore different tidal models (such as ADCIRC and TPXO) for further improvement of boundary conditions and accuracy of tide prediction in the Gulf. Finally, hurricane track and wind field are the most important forcing mechanisms but also the major sources of uncertainty for storm surge prediction. The time intervals of NOAA/HRD H*Wind (3 h) and hurricane track data (6 h) are generally not fine enough to capture sufficient detail in temporal variations of wind fields and will affect the accuracy of storm surge simulations. In addition, although the Holland method has been widely used in hurricane-induced storm surge simulations, it may be overly simplified in the region outside the core of hurricane. Different methods for improving hurricane wind fields can be explored in future study, such as optimization and data assimilation techniques (Dietrich et al. 2011), atmospheric model simulations (Davis et al. 2008), and parametric hurricane wind models (Shen et al. 2006; Chen et al. 2011).

Acknowledgements This study was funded by the Office of Biological and Environmental Research, Office of Science, US Department of Energy, under contract DE-AC05-76RL01830. The authors thank Dr. Changsheng Chen of the University of Massachusetts at Dartmouth and Dr. Virginia Burkett of the US Geological Survey. The authors would also like to thank the Coastal Protection and Restoration Authority of Louisiana for providing the subsidence data used in this study.

References

Bunya S, Dietrich JC, Westerink JJ, Ebersole BA, Smith JM, Atkinson JH (2010) A high-resolution coupled riverine flow, tide, wind, wind wave and storm surge model for Southern Louisiana and Mississippi:

- Part I: model development and validation. *Mon Weather Rev* 138:345–377. doi:[10.1175/2009MWR2906.1](https://doi.org/10.1175/2009MWR2906.1)
- Burkett VR, Hyman RC, Hagelman R, Hartley SB, Sheppard M, Doyle TW, Beagan DM, Meyers A, Hunt DT, Maynard MK, Henk RH, Seymour EJ, Olson LE, Potter JR, Srinivasan NN (2008) Why study the Gulf Coast? In: Savonis MJ, Burkett VR, Potter JR (eds) Impacts of climate change and variability on transportation systems and infrastructure: gulf coast study, phase I. A report by the US climate change science program and the subcommittee on global change research. Department of Transportation, Washington
- Chen C, Liu H, Beardsley RC (2003) An unstructured, finite-volume, three-dimensional, primitive equation ocean model: application to coastal ocean and estuaries. *J Atmos Ocean Technol* 20:159–186
- Chen C, Qi J, Li C, Beardsley RC, Lin H, Walker R, Gates K (2008) Complexity of the flooding/drying process in an estuarine tidal-creek salt-marsh system: an application of FVCOM. *J Geophys Res* 113:C07052. doi:[10.1029/2007jc004328](https://doi.org/10.1029/2007jc004328)
- Chen Q, Hu K, Kennedy A (2011) Numerical modeling of observed hurricane waves. *Coast Eng Proc* 1(32), waves.30. doi:[10.9753/icce.v32.waves.30](https://doi.org/10.9753/icce.v32.waves.30)
- Cho KH, Wang H, Shen J, Valle-Levinson A, Teng Y (2012) A modeling study on the response of the Chesapeake Bay to Hurricane Events of Floyd and Isabel. *Ocean Model* 49–50:22–46
- Coastal Protection and Restoration Authority of Louisiana (CPRA) (2012) Louisiana’s comprehensive master plan for a sustainable coast. Coastal Protection and Restoration Authority of Louisiana, Baton Rouge
- Davis CA, Wang W, Chen SS, Chen Y, Corbosiero K, DeMaria M, Dudhia J, Holland G, Klemp JB, Michalakes J, Reeves H, Rotunno R, Snyder CM, Xiao Q (2008) Prediction of landfalling hurricanes with the Advanced Hurricane WRF model. *Mon Weather Rev* 136:1990–2005. doi:[10.1175/2007MWR2085.1](https://doi.org/10.1175/2007MWR2085.1)
- Dawson C, Kubatko EJ, Westerink JJ, Trahan C, Mirabito C, Michoski C, Panda N (2011) Discontinuous Galerkin methods for modeling hurricane storm surge. *Adv Water Resour* 34:1165–1176. doi:[10.1016/j.advwatres.2010.11.004](https://doi.org/10.1016/j.advwatres.2010.11.004)
- Dietrich JC, Bunya S, Westerink JJ, Ebersole BA, Smith JM, Atkinson JH, Jensen R, Resio DT, Luettich RA, Dawson C, Cardone VJ, Cox AT, Powell MD, Westerink HJ, Roberts HJ (2010) A high-resolution coupled riverine flow, tide, wind, wind wave and storm surge model for Southern Louisiana and Mississippi: Part II—synoptic description and analyses of Hurricanes Katrina and Rita. *Mon Weather Rev* 138:378–404. doi:[10.1175/2009MWR2907.1](https://doi.org/10.1175/2009MWR2907.1)
- Dietrich JC, Zijlema M, Westerink JJ, Holthuijsen LH, Dawson CN, Luettich RA Jr, Jensen RE, Smith JM, Stelling GS, Stone GW (2011) Modeling hurricane waves and storm surge using integrally-coupled, scalable computations. *Coast Eng* 58:45–65
- Dixon TH, Amelung F, Ferretti A, Novali F, Rocca F, Dokka R, Sellall G, Kim S-W, Wdowinski S, Whitman D (2006) Subsidence and flooding in New Orleans. *Nature* 441:587–588
- Gornitz V, White TW, Cushman RM (1991) Vulnerability of the US to future sea-level rise. *Coastal Zone* 91, 2354–2368. In: Proceedings of seventh symposium on coastal and ocean management. American Society of Civil Engineers
- Gouillon F, Morey SL, Dukhovskoy DS, O’Brien JJ (2010) Forced tidal response in the Gulf of Mexico. *J Geophys Res* 115:C10050. doi:[10.1029/2010JC006122](https://doi.org/10.1029/2010JC006122)
- Graumann A, Houston T, Lawrimore J, Levinson D, Lott N, McCown S, Stephens S, Wuertz D (2005) Hurricane Katrina, a climatological perspective. NOAA’s National Climatic Data Center Technical Report 2005-01
- Hill DF, Griffiths SD, Peltier WR, Horton BP, Törnqvist TE (2011) High-resolution numerical modeling of tides in the western Atlantic, Gulf of Mexico, and Caribbean Sea during the Holocene. *J Geophys Res* 116:C10014. doi:[10.1029/2010JC006896](https://doi.org/10.1029/2010JC006896)
- Holland GJ (1980) An analytic model of the wind and pressure profiles in hurricanes. *Mon Weather Rev* 108:1212–1218
- Irish JL, Resio D, Ratcliff JJ (2008) The influence of storm size on hurricane surge. *J Phys Oceanogr* 38:2003–2013
- Ji R, Ashjian C, Campbell R, Chen C, Gao G, Davis CS, Cowles G, Beardsley RC (2011) Life history and biogeography of *Calanus* copepod in the Arctic Ocean: an individual-based modeling study. *Prog Oceanogr* 96(40–56):2011. doi:[10.1016/j.pocean.10.001](https://doi.org/10.1016/j.pocean.10.001)
- Karsten LK, McMillian JM, Lickley MJ (2008) Assessment of tidal current energy in Minas Passage, Bay of Fundy. *Proc Inst Mech Eng Part A* 222:493–507. doi:[13-80/282JP5366](https://doi.org/10.1380/282JP5366)
- Kennedy AB, Westerink JJ, Smith JM, Hope ME, Hartman M, Taflanidis A, Tanaka S, Westerink H, Cheung K, Smith T, Hamann M, Minamide M, Ota A, Dawson C (2012) Tropical cyclone inundation potential on the Hawaiian Islands of Oahu and Kauai. *Ocean Model* 52–53:54–68

- Lai Z, Chen C, Beardsley RC, Rothschild B, Tian R (2010a) Impact of high-frequency nonlinear internal waves on plankton dynamics in Massachusetts Bay. *J Mar Res* 68:259–281
- Lai Z, Chen C, Cowles G, Beardsley RC (2010b) A non-hydrostatic version of FVCOM. Part II: mechanistic study of tidally generated nonlinear internal waves in Massachusetts Bay. *J Geophys Res* 115(49):1–21
- Large WG, Pond S (1981) Open ocean momentum flux measurements in moderate to strong winds. *J Phys Oceanogr* 11:324–336
- Luettich RA, Westerink JJ, Scheffner NW (1992) ADCIRC: an advanced three dimensional circulation model for shelves, coasts and estuaries. Report 1: Theory and methodology of ADCIRC-2DDI and ADCIRC-3DL. Dredging Research Program Technical Report DRP-92-6, U.S. Army Engineers Waterways Experiment Station, Vicksburg, MS
- Mariotti G, Fagherazzi S, Wiberg PL, McGlathery KJ, Carniello L, Defina A (2010) Influence of storm surges and sea level on shallow tidal basin erosive processes. *J Geophys Res* 115:C11012. doi:[10.1029/2009JC005892](https://doi.org/10.1029/2009JC005892)
- Meehl GA, Stocker TF, Collins WD, Friedlingstein P, Gaye AT, Gregory JM, Kitoh A, Knutti R, Murphy JM, Noda A, Raper SCB, Watterson IG, Weaver AJ, Zhao Z-C (2007) Global climate projections. In: Solomon S, Qin D, Manning M, Chen Z, Marquis M, Averyt KB, Tignor M, Miller HL (eds) *Climate Change 2007: The physical science basis contribution of working Group I to the fourth assessment Report of the intergovernmental panel on climate change*. Cambridge University Press, Cambridge, pp 747–845
- Minerals Management Service (2006) Impact Assessment of Offshore Facilities from Hurricanes Katrina and Rita, News Release 3486, May 1, 2006
- Mousavi ME, Irish JL, Frey AE, Olivera F, Edge BL (2010) Global warming and hurricanes: the potential impact of hurricane intensification and sea level rise on coastal flooding. *Clim Change* 104(3–4): 575–597
- Needham H, Brown D, Carter L (2012) Impacts and adaptation options in the Gulf Coast. Center for Climate and Energy Solutions, Arlington, VA, <http://www.c2es.org/docUploads/gulf-coast-impacts-adaptation.pdf>
- Nicholls RJ, Wong PP, Burkett VR, Codignotto JO, Hay JE, McLean RF, Ragoonaden S, Woodroffe CD (2007) Coastal systems and low-lying areas. In: Parry ML, Canziani OF, Pauutikof JP, van der Linden PJ, Hanson CE (eds) *Climate Change 2007: Impacts, Adaptation and Vulnerability. Contribution of Working Group II to the Fourth Assessment Report of the Intergovernmental Panel on Climate Change*. Cambridge University Press, Cambridge, pp 315–356
- Nicholls RJ, Hanson S, Lowe JA, Warrick RA, Lu X, Long AJ, Carter TA (2011) Constructing sea-level scenarios for impact and adaptation assessment of coastal areas: a guidance document. Supporting Material, Intergovernmental Panel on Climate Change Task Group on Data and Scenario Support for Impact and Climate Analysis (TGICA), Geneva, Switzerland, 47 pp
- NOAA/NWS. 2012. Tropical cyclone definition. Tropical Cyclone Weather Services Program, NWS PD 10-6, <http://www.nws.noaa.gov/directives/sym/pd01006004curr.pdf>
- Pendleton EA, Barras JA, Williams SJ, Twichell DC (2010) Coastal vulnerability assessment of the Northern Gulf of Mexico to sea-level rise and coastal change. U.S. Geological Survey Open-File Report 2010-1146, <http://pubs.usgs.gov/of/2010/1146/>
- Pfeffer WT, Harper JT, O'Neel S (2008) Kinematic constraints on glacier contributions to 21st-century sea-level rise. *Science* 321:1340–1343
- Powell MD, Houston SH, Amat LR, Morisseau-Leroy N (1998) The HRD real-time hurricane wind analysis system. *J Wind Eng Ind Aerodyn* 77&78:53–64
- Powell MD, Murillo S, Dodge P, Uhlhorn E, Gamache J, Cardone V, Cox A, Otero S, Carrasco N, Annane B, St Fleur R (2010) Reconstruction of Hurricane Katrina's wind fields for storm surge and wave hindcasting. *Ocean Eng* 37:26–36
- Shen J, Zhang K, Xiao C, Gong W (2006) Improved prediction of storm surge inundation using a high-resolution unstructured grid model. *J Coastal Res* 22:1309–1319. doi:[10.2112/04-0288.1](https://doi.org/10.2112/04-0288.1)
- Sheng YP, Alymov V, Paramygin VA (2010) Simulation of storm surge, wave, currents, and inundation in the Outer Banks and Chesapeake Bay during Hurricane Isabel in 2003: the importance of waves. *J Geophys Res* 115(C04008):1–27. doi:[10.1029/2009JC00](https://doi.org/10.1029/2009JC00)
- Staudt A, Curry R (2011) More extreme weather and the U.S. energy infrastructure. Natl Wildl Federation, Report, p 16
- Tebaldi C, Strauss BH, Zervas CE (2012) Modelling SLR impacts on storm surges along US coasts. *Environ Res Lett* 7:014032. doi:[10.1088/1748-9326/7/1/014032](https://doi.org/10.1088/1748-9326/7/1/014032)
- Thieler ER, Hammar-Klose ES (2000) National assessment of coastal vulnerability to future sea-level rise: preliminary results for the U.S. Gulf of Mexico Coast. U.S. Geological Survey, Open-File Report 00-179, <http://pubs.usgs.gov/of/of00-179/>

- Vermeer M, Rahmstorf S (2009) Global sea level linked to global temperature. *Proc Natl Acad Sci USA* 106:21527–21532
- Wang T, Yang Z, Copping A (2013) A modeling study of the potential water quality impacts from in-stream tidal energy extraction. *Estuaries and Coasts*. doi:[10.1007/s12237-013-9718-9](https://doi.org/10.1007/s12237-013-9718-9)
- Warner NN, Tissot PE (2012) Storm flooding sensitivity to SLR for Galveston Bay, Texas. *Ocean Eng* 44:23–32
- Weisberg RH, Zheng L (2006) Hurricane storm surge simulations for Tampa Bay. *Estuaries Coasts* 29:899–913
- Weisberg RH, Zheng L (2008) Hurricane storm surge simulations comparing three-dimensional with two-dimensional formulations based on an ivan-like storm over the Tampa Bay, Florida Region. *J Geophys Res* 113:C12001. doi:[10.1029/2008JC005115](https://doi.org/10.1029/2008JC005115)
- Westerink JJ, Luettich RA Jr, Feyen JC, Atkinson JH, Dawson C, Powell MD, Dunion JP, Roberts HJ, Kubatko EJ, Pourtaheri H (2008) A basin- to channel- scale unstructured grid hurricane storm surge model as implemented for Southern Louisiana. *Mon Weather Rev* 136:833–864. doi:[10.1175/2007MWR1946.1](https://doi.org/10.1175/2007MWR1946.1)
- Willis JK, Church JA (2012) Regional Sea-level projection. *Science* 336:550. doi:[10.1126/science.1220366](https://doi.org/10.1126/science.1220366)
- Xing J, Davies AM, Jones E (2011) Application of an unstructured mesh model to the determination of the baroclinic circulation of the Irish Sea. *J Geophys Res* 116:C10026. doi:[10.1029/2011JC007063](https://doi.org/10.1029/2011JC007063)
- Xu H, Zhang K, Shen J, Li Y (2010) Storm surge simulation along the U.S. East and Gulf Coasts using a multi-scale numerical model approach. *Ocean Dyn* 60:1597–1619. doi:[10.1007/s10236-010-0321-3](https://doi.org/10.1007/s10236-010-0321-3)
- Yang Z, Wang T (2013) Tidal residuals, eddies and their effects on water exchange in puget sound. *Ocean Dyn* 63:995–1009. doi:[10.1007/s10236-013-0635-z](https://doi.org/10.1007/s10236-013-0635-z)
- Yang Z, Wang T, Khangaonkar T, Breithaupt S (2012) Integrated modeling of flood flows and tidal hydrodynamics over a coastal floodplain. *J Environ Fluid Mech* 12:63–80. doi:[10.1007/s10652-011-9214-3](https://doi.org/10.1007/s10652-011-9214-3)
- Yang Z, Wang T, Copping A (2013) Modeling tidal stream energy extraction and its effects on transport processes in a tidal channel and bay system using a three-dimensional coastal ocean model. *Renew Energy* 50:605–613. doi:[10.1016/j.renene.2012.07.024](https://doi.org/10.1016/j.renene.2012.07.024)
- Zheng L, Weisberg RH (2012) Modeling the west Florida coastal ocean by downscaling from the deep ocean, across the continental shelf and into the estuaries. *Ocean Model* 48:10–29